**ICES Report 04-60**

# A FEW NEW (?) FACTS ABOUT INFINITE ELEMENTS

L. Demkowicz[a], Jie Shen[b]

[a]**Institute for Computational Engineering and Sciences**
**The University of Texas at Austin**

[b]**Department of Mathematics**
**Purdue University**

**Abstract**

We discuss the (conjugated) Bubnov-Galerkin and Petrov-Galerkin Infinite Element (IE) discretizations to Helmholtz equation including stability, use of locally variable order, optimal choice of IE shape functions, calculation of Radar Cross Sections (RCS), and automatic $hp$-adaptivity. The discussions are complemented with 2D numerical experiments.

**Key words:** Helmholtz equation, infinite element, $hp$ finite elements, RCS

**AMS subject classification:** 65N30, 35L15

### Acknowledgment

The work of the first author has been supported by Air Force under Contract FA9550-04-1-0050 while that of the second-order is partially supported by NSF grant DMS-0311915.

## 1 Introduction

We will not attempt any comprehensive review of infinite elements. The technology has long been in place, has enjoyed a tremendous progress and a large number of research papers in the recent years, and it remains at forefront of challenging research, see e.g. [2].

This short contribution has been motivated with the idea of the second author who, several years ago, suggested to employ rational functions generated from the (integrated) Jacobi polynomials as infinite element shape functions. The issue resurfaced recently in context of using the infinite element for solving exterior Maxwell problems and determining Radar Cross Sections (RCS) [13]. Apparently, the IE elements have suffered from poor conditioning, especially for non-spherical truncating surfaces. The issue has been reported in the acoustics community as well, see e.g. [11].

In process of putting together a short chapter on $hp$-adaptivity for exterior boundary value problems [4], the first author has learned a few extra new (at least for him) facts that might be useful to the IE community. Those include the following issues.

- The possibility of using the same shape trial and test functions for the conjugated infinite element. To our best knowledge, a complete convergence proof for any infinite element technology remains an open issue (cf. [5]). Symmetry of the formulation makes, in general, the stability analysis easier, and can be exploited in designing optimal linear solvers.
- The possibility of a uniform formulation for both 2D and 3D problems.
- The possibility of varying locally the IE spectral order of approximation.
- The possibility of a direct evaluation of RCS, without any costly post-processing.

The final motivation came from an early investigation of the effect of resolving singularities in the field on the accuracy of RCS calculations, aimed at developing a general technology combining the goal-driven automatic $hp$-adaptivity [12, 10] with infinite elements. The automatic $hp$-adaptivity allows for an unprecedented accuracy of simulations. The question is : "Is this technology really necessary for accurate RCS predictions?"

## 2 Formulation of the problem

We shall consider the exterior boundary value problem for the Helmholtz equation, representing a class of acoustical rigid scattering problems.

Let $\Omega_{int}$ be an open bounded domain in $\mathbb{R}^n$, we set $\Omega = \mathbb{R}^n - \bar{\Omega}_{int}$. Given an *incident pressure wave* $u^{inc}$ that satisfies the Helmholtz equation in the whole space,

$$-\Delta u^{inc} - k^2 u^{inc} = 0 \quad \text{in } \mathbb{R}^n \,,$$

we look for a *scattered pressure wave* $u$ that satisfies:

- the same Helmholtz equation, but only in the exterior domain,

$$-\Delta u - k^2 u = 0 \quad \text{in } \Omega = \mathbb{R}^n - \Omega_{int} \,,$$

- Neumann boundary condition on boundary $\Gamma = \partial\Omega = \partial\Omega_{int}$,

$$\frac{\partial(u + u^{inc})}{\partial n} = 0 \,,$$

- Sommerfeld radiation condition at infinity,

$$\frac{\partial u}{\partial r} + iku \in L^2(\Omega) \,.$$

Here $k = \frac{\omega}{c} > 0$ is the wave number with $\omega$ representing the angular frequency, and $c$ the speed of sound in the (homogeneous) medium, $\boldsymbol{n}$ is the outward unit vector, and $r$ stands for the radial coordinate corresponding to polar coordinates with the origin at an arbitrary point, typically chosen inside of the interior domain $\Omega_{int}$ occupied by the rigid obstacle (scatterer). As the gradient of the pressure is proportional to the velocity vector, the Neumann boundary condition corresponds to the requirement that the normal component of the total velocity vector must vanish on the boundary of the rigid obstacle. The sum of the incident and scattered pressures represents the total pressure wave. In practice, the incident pressure wave corresponds to a source located away from the obstacle. If the location of the source is far enough, the incident pressure wave may be assumed in the form of a plane wave (source at infinity),

$$u^{inc}(\boldsymbol{x}) = u_0 e^{ik\boldsymbol{e}\cdot\boldsymbol{x}} ,$$

where $u_0$ is a scaling factor, and unit vector $\boldsymbol{e}$ represents the direction of the incoming incident wave. As the problem is linear, we can assume $u_0 = 1$. The role of the incident wave is therefore to provide only a driving Neumann load data on boundary $\Gamma$,

$$\frac{\partial u}{\partial n} = g := -\frac{\partial u^{inc}}{\partial n} . \tag{2.1}$$

The Sommerfeld radiation condition represents a requirement that the scattered wave must be *outgoing* to infinity, and it can be represented in many different but equivalent forms. The form used here has a particular advantage of being independent of space dimension.

Notice that the sign in the Sommerfeld radiation condition corresponds to the $e^{i\omega t}$ ansatz in time.

Of particular interest to us, will be the computation of the monostatic *Radar Cross Section* (RCS) defined as,

$$\lim_{r\to\infty} |u(r\hat{\boldsymbol{x}})\ | r^{\alpha} . \tag{2.2}$$

Here $\hat{\boldsymbol{x}}$ is a point on the unit sphere (circle) specifying the direction of the incident wave, $\boldsymbol{e} = \hat{\boldsymbol{x}}$, and $u$ is the corresponding scattered wave. Coefficient,

$$\alpha = \begin{cases} \frac{1}{2} & \text{in } \mathbb{R}^2 \\ 1 & \text{in } \mathbb{R}^3 \end{cases}$$

reflects the decay rate of the leading term (far field pattern) in the solution.

# 3 Infinite element discretization

## 3.1 Scattering on a cylinder (sphere)

Introducing the variational formulation for an exterior problem is different from the standard construction for bounded domains. We will begin our discussion with a special case of a cylindrical (spherical in 3D) scatterer of radius $a$.

We surround the scatterer with a larger circle (sphere in 3D) of radius $R$, and follow the standard derivation of the variational formulation for the truncated exterior domain,

$$\Omega_R = \{\boldsymbol{x} \,:\, a < |\boldsymbol{x}| < R\} \,.$$

Assuming $u, v \in H^1(\Omega_R)$, we obtain,

$$\int_{\Omega_R} \{\boldsymbol{\nabla} u \boldsymbol{\nabla} \bar{v} - k^2 u \bar{v}\} \, d\boldsymbol{x} + ik \int_{S_R} u \bar{v} \, ds = \int_\Gamma g \bar{v} \, ds + \int_{S_R} w \bar{v} \, ds, \quad \forall v \,. \tag{3.3}$$

Here $w := \frac{\partial u}{\partial r} + iku$, according to the Sommerfeld condition, denotes an unknown $L^2$ function, and $\Gamma$ is the boundary of the scatterer i.e., in this case, $\Gamma = S_a$.

We want to pass $R \to +\infty$ in (3.3). $L^2$-integrability of function $w$ implies that the unknown term will vanish. The first boundary integral on the right-hand side is independent of $R$, so we only need to focus on the two integrals on the left-hand side only.

We shall use the following curvilinear coordinates, corresponding to the finite element implementation,

$$\boldsymbol{x}(r, \xi) = r \boldsymbol{x}_a(\xi), \quad r > 1, \quad |\boldsymbol{x}_a| = a \,,$$

where $\boldsymbol{x}_a(\xi)$ denotes a parametrization of the circle (sphere in 3D) of radius $a$. We have the standard formulas,

$$\begin{aligned}
&\frac{\partial \boldsymbol{x}}{\partial r} = \boldsymbol{x}_a = a \boldsymbol{e}_r, \text{ where } \boldsymbol{e}_r := a^{-1} \boldsymbol{x}_a, \\
&\frac{\partial \boldsymbol{x}}{\partial \xi} = r \, \frac{\partial \boldsymbol{x}_a}{\partial \xi} = r |\frac{\partial \boldsymbol{x}_a}{\partial \xi}| \, \boldsymbol{e}_\xi, \text{ where } \boldsymbol{e}_\xi := |\frac{\partial \boldsymbol{x}}{\partial \xi}|^{-1} \frac{\partial \boldsymbol{x}}{\partial \xi} \,, \\
&\boldsymbol{\nabla} u = \frac{1}{a} \frac{\partial u}{\partial r} \boldsymbol{e}_r + \underbrace{\frac{1}{r} \frac{\partial u}{\partial \xi} |\frac{\partial \boldsymbol{x}_a}{\partial \xi}|^{-1} \boldsymbol{e}_\xi}_{\boldsymbol{\nabla}_{S_a} u} = \frac{\partial u}{\partial r} \boldsymbol{e}_r + \frac{1}{r} \boldsymbol{\nabla}_{S_a} u \,,
\end{aligned}$$

with $\boldsymbol{\nabla}_{S_a}$ denoting the gradient on the circle (sphere) $S_a$.

**Separation of variables**

We shall exploit the separability of the domain by assuming the solution $u$ and the test function $v$ in the standard form,

$$u(r, \boldsymbol{x}_a) = \sum_\iota U_\iota(r) \psi_\iota(\boldsymbol{x}_a), \quad v(r, \boldsymbol{x}_a) = \sum_\kappa V_\kappa(r) \phi_\kappa(\boldsymbol{x}_a) \,.$$

In the following, we will drop indices $\iota, \kappa$ and focus on the integrability of a single term. On the discrete level, each term will correspond to an entry in the global stiffness matrix.

Separation of variables leads to the following formula for the domain integral,

$$\begin{aligned}
a^{-1} \left\{ \int_1^\rho (U' \bar{V}' - (ka)^2 U \bar{V}) \, r^\alpha dr + ika \, \rho^\alpha \, U(\rho) \bar{V}(\rho) \right\} \int_{S_a} \psi \bar{\phi} \, dS_a \\
+ a \int_1^\rho \frac{1}{r^2} U \bar{V} \, r^\alpha dr \int_{S_a} \boldsymbol{\nabla}_{S_a} \psi \boldsymbol{\nabla}_{S_a} \bar{\phi} \, dS_a \,,
\end{aligned}$$

where $\rho a = R$, $\alpha = 1$ for 2D, and $\alpha = 2$ for 3D problems. We shall discuss now sufficient conditions for Lebesgue integrability of terms,

$$\begin{array}{l} \displaystyle\int_1^\infty (U'\bar{V}' - (ka)^2 U\bar{V})\, r^\alpha dr, \\ \displaystyle\int_1^\infty \frac{1}{r^2} U\bar{V}\, r^\alpha dr\ . \end{array} \tag{3.4}$$

and the existence of the limit,

$$\lim_{\rho\to\infty} \rho^\alpha\, U(\rho)\bar{V}(\rho)\ . \tag{3.5}$$

**Step 1: Taking out the oscillating factor.** The formula for the exact solution (cf. [9]) suggests building into the solution ansatz, the oscillating factor $e^{ikar}$. "Overloading" symbols $U$ and $V$, we introduce,

$$\begin{array}{ll} U(r) \stackrel{'}{=} e^{-ika(r-1)}U(r), & \bar{V}(r) \stackrel{'}{=} e^{ika(r-1)}\bar{V}(r) \\ U' \stackrel{'}{=} (U' - ikaU)e^{-ika(r-1)}, & \bar{V}' \stackrel{'}{=} (\bar{V}' + ika\bar{V})e^{ika(r-1)}\ . \end{array}$$

This leads to the following modifications of the integrands (3.4) and the boundary term (3.5),

$$\begin{aligned} U'\bar{V}' - (ka)^2 U\bar{V} &\stackrel{'}{=} U'\bar{V}' + ika(U'\bar{V} - U\bar{V}') \\ \frac{1}{r^2}U\bar{V} &\stackrel{'}{=} \frac{1}{r^2}U\bar{V} \\ \rho^\alpha\, U(\rho)\bar{V}(\rho) &\stackrel{'}{=} \rho^\alpha\, U(\rho)\bar{V}(\rho)\ . \end{aligned}$$

**Step 2: Taking out the Jacobian.** In an effort to make the formulation dimension independent, our second modification of the ansatz for the solution and the test function, involves an additional factor corresponding to the Jacobian $r^\alpha$, where $\alpha = 1$ for 2D, and $\alpha = 2$ for 3D problems. "Overloading" symbols $U, V$ again, we have,

$$\begin{array}{ll} U \stackrel{'}{=} r^{-\alpha/2}U, & \bar{V} \stackrel{'}{=} r^{-\alpha/2}\bar{V}, \\ U' \stackrel{'}{=} (U' - \frac{\alpha}{2r}U)r^{-\alpha/2}, & \bar{V}' \stackrel{'}{=} (\bar{V}' - \frac{\alpha}{2r}\bar{V})r^{-\alpha/2}\ . \end{array}$$

This leads to the following modification of the terms of interest,

$$\begin{aligned} \left\{U'\bar{V}' + ika(U'\bar{V} - U\bar{V}')\right\} r^\alpha &\stackrel{'}{=} U'\bar{V}' - \frac{\alpha}{2r}(U\bar{V})' + \frac{\alpha^2}{4r^2}U\bar{V} + ika(U'\bar{V} - U\bar{V}') \\ \left\{\frac{1}{r^2}U\bar{V}\right\} r^\alpha &\stackrel{'}{=} \frac{1}{r^2}U\bar{V} \\ \rho^\alpha U(\rho)\bar{V}(\rho) &\stackrel{'}{=} U(\rho)\bar{V}(\rho) \end{aligned}$$

Term $(U\bar{V})'$ can be eliminated by integrating by parts,

$$-\frac{\alpha}{2}\int_1^\infty \frac{1}{r}(U\bar{V})'\, dr = -\frac{\alpha}{2}\int_1^\infty \frac{1}{r^2}U\bar{V}\, dr + \frac{\alpha}{2}U(1)\bar{V}(1)\ .$$

The final form of the two terms contributing to the domain integral becomes,

$$\begin{aligned}\int_1^\infty U'\bar{V}'\,dr + \frac{\alpha}{2}\left(\frac{\alpha}{2}-1\right)\int_1^\infty \frac{1}{r^2}\,U\bar{V}\,dr + \frac{\alpha}{2}U(1)\bar{V}(1)\\ +ika\left[\int_1^\infty (U'\bar{V}-U\bar{V}')\,dr + \lim_{\rho\to\infty} U(\rho)\bar{V}(\rho)\right],\end{aligned} \tag{3.6}$$

and,

$$\int_1^\infty \frac{1}{r^2}U\bar{V}\,dr\,, \tag{3.7}$$

where symbols $U$ and $V$ correspond to the contributions on the right hand side of the formulas,

$$\begin{aligned}U(r) &\overset{'}{=} r^{-\alpha/2}e^{-ika(r-1)}U(r)\,,\\ \bar{V}(r) &\overset{'}{=} r^{-\alpha/2}e^{ika(r-1)}\bar{V}(r)\,.\end{aligned}$$

**Step 3: Selecting radial shape functions.** The formula for the exact solution suggests selecting,

$$U \approx U_N = u_0 + \frac{1}{r}u_1 + \ldots + \frac{1}{r^N}u_N\,, \tag{3.8}$$

where $u_1,\ldots,u_N$ are unknown coefficients.

The test functions may be selected in different ways. We shall discuss two most natural choices.

**Same trial and test functions (Bubnov-Galerkin)**

$$V \approx V_N = v_0 + \frac{1}{r}v_1 + \ldots + \frac{1}{r^N}v_N\,,$$

Notice that,

- all integrals in (3.6) and (3.7) are well defined;
- $\lim_{\rho\to\infty} U(\rho)\bar{V}(\rho) = u_0\bar{v}_0$

**Different trial and test functions (Petrov-Galerkin)**

$$V \approx V_N = \frac{1}{r^\alpha}\left\{v_0 + \frac{1}{r}v_1 + \ldots + \frac{1}{r^N}v_N\right\}\,,$$

In this case,

- all integrals in (3.6) and (3.7) are well defined;
- $\lim_{\rho\to\infty} U(\rho)\bar{V}(\rho) = 0$

The symmetric formulation is possible due to the interpretation of the domain integral in the Cauchy Principal Value (CPV) sense. We first integrate over the truncated domain, then *allow for the cancellation of Lebesgue non-summable terms* (cf. Step 1 of the derivation), and only then pass to the limit with $\rho\to\infty$. For

the second choice of the test functions, all integrals contributing to the sesquilinear form exist independently. In the three- dimensional case, we can also make an intermediate choice,

$$V \approx V_N = \frac{1}{r}\left\{v_0 + \frac{1}{r}v_1 + \ldots + \frac{1}{r^N}v_N\right\} .$$

In this case, the integrals have to also be understood in the CPV sense.

We will present numerical results for both formulations.

### 3.2 Conditioning and optimal shape functions.

Selecting functions $1/r^n$ for radial shape functions results in poor conditioning as the functions are "too similar" to each other. In order to make a better choice, we first make the change of variables,

$$r = \frac{1}{x}, \quad dr = -\frac{1}{x^2}\,dx, \quad \frac{dU}{dr} = -x^2\frac{dU}{dx} .$$

Then, integrals (3.6), (3.7) transform into,

$$\begin{aligned}\int_0^1 x^2\, U'\bar{V}'\, dx + \frac{\alpha(\alpha-2)}{4}\int_0^1 U\bar{V}\, dx + \frac{\alpha}{2}U(1)\bar{V}(1) \\ -ika\left[\int_0^1 (U'\bar{V} - U\bar{V}')\, dx - U(0)\bar{V}(0)\right] ,\end{aligned} \tag{3.9}$$

and,

$$\int_0^1 U\bar{V}\, dx . \tag{3.10}$$

The leading term (derivative times derivative) is most responsible for the conditioning problems, and it motivates our choice of radial shape functions to be integrals of Jacobi polynomials $P_n^{(2,0)}(2x-1)$, which, thanks to the orthogonality of the Jacobi polynomials, are mutually orthogonal with respect to the first integral in (3.9) and hence will lead to better-conditioned linear system. We note that the approximation properties of the associated (through the transform $x = \frac{1}{r}$) rational functions $R_n(r) := P_n^{(2,0)}(\frac{2}{r} - 1)$ and their applications for solving elliptic equations in exterior domains were studied in [8].

### 3.3 Scatterers of an arbitrary shape.

For a scatterer of an arbitrary shape, the formulation is identical to the special scatter considered above. Meshing the exterior domain involves introducing a truncating sphere (circle) of radius $a$ - $S_a$ with $a$ usually selected in such a way that the distance of $S_a$ from the scatterer does not exceed one wave length. The space between the scatterer and the truncating sphere is then meshed with finite element. Each finite element face (edge in 2D) on the truncating sphere gives then rise to a separate infinite element. The technique can be extended to ellipsoidal (elliptic) truncating surfaces, see the illustration of the concept in Fig. 1.

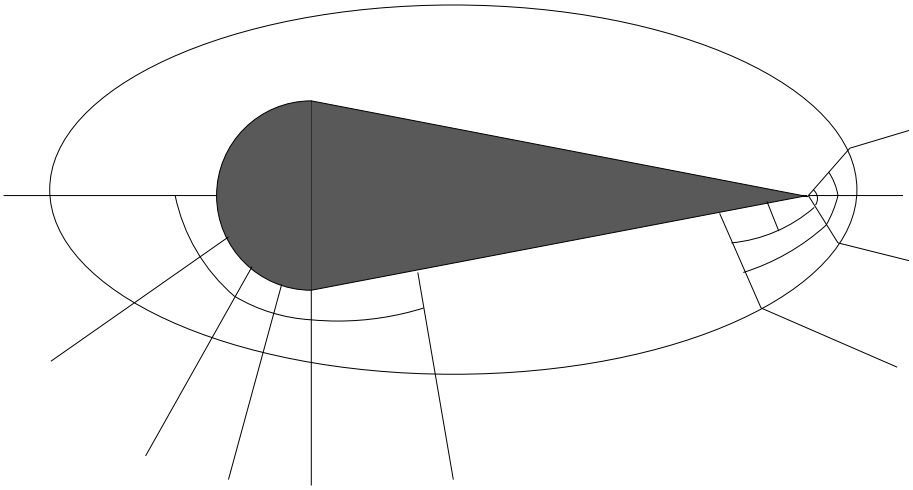

Figure 1: FE/IE mesh around a scatterer

# 4 Implementation

We proceed now with a short description of the implementation of the described discretization within the *2Dhp* - the two-dimensional $hp$ code, supporting automatic $hp$-adaptivity [7, 4].

## 4.1 Data structure, interface with frontal solver

Conceptually, infinite elements may be treated the same way as finite elements. Shape-wise, in 2D, they fall into the category of quads. The corresponding shape functions are defined as tensor products of 1D shape functions, same way as for the standard quadrilaterals, except for the logic on nodes and the corresponding nodal connectivities. In 2D, each infinite element has only two vertex nodes, one mid-edge node on the truncating circle, the middle node, and two mid-edge nodes on the radial edges originating from the vertex nodes on the truncating circle.

Thus, one way to code the infinite elements, would be to add a new element type to the code, and develop then all necessary data structure, constrained approximation (in 3D only), mesh refinements, and mesh optimization routines.

We follow the philosophy of our previous implementations [3], and choose a simpler way, based on treating the infinite elements as an (implicit) form of an Absorbing Boundary Condition (ABC). Instead of setting up a permanent data structure, we generate a *temporary data* every time, the problem on the FE/IE mesh is solved. The resulting infinite element d.o.f. are then stored in the temporary data structure arrays, and can be used for visualization or post-processing. The moment, however, any finite element adjacent to the truncating surface is modified, the content of the IE data structure arrays becomes meaningless.

The temporary IE data structure arrays, stored in *module/infinite_elements*, include three arrays. Arrays

*IELEMS* and *IENODS* store new objects:

- type *infinite element*,
- type *infinite element node*.

The attributes of an infinite element include,

- the element nodes listed in the order: middle node, left radial mid-edge node, right radial mid-edge node, the mid-edge node on the truncating circle, left vertex, and right vertex nodes,
- the orientation of the mid-edge node on the truncating circle.

The attributes of an infinite element mode are similar to those of the standard nodes. The include node type (*medg* or *mdlq*), order of the node. and the corresponding degrees of freedom *zdofs*.

The third, integer array, *ELTOIE*, is dimensioned with *MAXNODS* - the maximum number of FE higher order nodes. The array is populated with zeros except for entries corresponding to middle nodes of elements adjacent to the truncating surface which store the adjacent infinite element numbers.

The edges located on the truncating circle are flagged in the input file with (boundary condition) *BC flag* = 9. The infinite elements are generated then in the order in which the edges with the *BC flag* = 9, are encountered, following the *natural order of elements*. In other words, in presence of infinite elements, the natural order of elements is modified, by "inserting" infinite elements after the adjacent finite elements.

Finally, in presence of infinite elements, the interface with the frontal solver must be modified.

Please visit the source code for details.

## 4.2 Calculation of infinite element stiffness matrix. The infinite element routine

As discussed in the previous section, the infinite elements shape functions are tensor products of FE shape functions and IE *radial* shape functions. We begin with a parametrization for the edge adjacent to the truncating circle,

$$\boldsymbol{x}_e(\xi_1), \xi_1 \in (0,1) \; . \tag{4.11}$$

In practice, we replace the exact circle with its isoparametric FE approximation,

$$\boldsymbol{x}_e(\xi_1) = \boldsymbol{x}_1(1-\xi_1) + \boldsymbol{x}_2\xi_1 + \sum_{j=1}^{p-1} \boldsymbol{x}_{3,j}\hat{\chi}_{3,j}(\xi_1) \; . \tag{4.12}$$

Here $\hat{\chi}_{3,j}(\xi_1)$ denote the mid-edge node (1D master element) shape functions of order $p$, $\boldsymbol{x}_1, \boldsymbol{x}_2$ are the vertex nodes coordinates, and $\boldsymbol{x}_{3,j}$ denote the mid-edge node geometry d.o.f.

The mapping from the *infinite master element* occupying the standard unit square, can then be described as,

$$\boldsymbol{x} = \boldsymbol{x}(\xi_1, \xi_2) = \boldsymbol{x}_e(\xi_1)\frac{1}{\xi_2} \; .$$

Notice that the edge $\xi_2 = 0$ corresponds to the infinity. The IE trial shape functions are defined then as,

$$\psi_{ik}(\boldsymbol{x}) = \hat{\chi}_i(\xi_1)\, \xi_2^{1/2} e^{-ika(\frac{1}{\xi_2}-1)} \hat{\psi}_k(\xi_2)\,, \tag{4.13}$$

where the radial shape functions are defined as the integrals of the Jacobi polynomials $P_n^{(2,0)}$ (transformed to interval (0,1)),

$$\psi_j(\xi) = \begin{cases} 1 & j = 1 \\ \dfrac{\int_\xi^1 P_{j-2}^{(2,0)}(2t-1)\, dt}{\int_0^1 P_{j-2}^{(2,0)}(2t-1)\, dt} & j > 1\,. \end{cases} \tag{4.14}$$

The infinite element test shape functions are identical with the trial shape functions for the Bubnov-Galerkin version, and for the Petrov-Galerkin scheme they are given by,

$$\phi_{ika}(\boldsymbol{x}) = \hat{\chi}_i(\xi_1)\, \xi_2^{1/2} e^{-ika(\frac{1}{\xi_2}-1)} \hat{\phi}_k(\xi_2)\,, \tag{4.15}$$

where the radial test functions are computed according to,

$$\psi_j(\xi) = \begin{cases} \dfrac{\int_0^\xi P_0^{(2,0)}(2t-1)\, dt}{\int_0^1 P_0^{(2,0)}(2t-1)\, dt} & j = 1 \\ \dfrac{\int_\xi^1 P_{j-1}^{(2,0)}(2t-1)\, dt}{\int_0^1 P_{j-1}^{(2,0)}(2t-1)\, dt} & j > 1\,. \end{cases} \tag{4.16}$$

The computation of the infinite element stiffness matrix is reduced to evaluation of four "one-dimensional" matrices [1]

$$\int_K \{\boldsymbol{\nabla}\psi_{ika}\boldsymbol{\nabla}\bar{\phi}_{jl} - k^2\psi_{ika}\bar{\phi}_{jl}\}\, d\boldsymbol{x} = a^{-1}\, S_{ij}^1 R_{kl}^1 + a\, S_{ij}^2 R_{kl}^2\,. \tag{4.17}$$

Here $S_{ij}^1, S_{ij}^2$ denote "1D curved finite element" matrices,

$$\begin{aligned} S_{ij}^1 &= \int_0^1 \hat{\chi}_i(\xi)\hat{\chi}_j(\xi)\frac{ds}{d\xi}\, d\xi \\ S_{ij}^2 &= \int_0^1 \hat{\chi}_i'(\xi)\hat{\chi}_j'(\xi)(\frac{ds}{d\xi})^{-1}\, d\xi\,, \end{aligned} \tag{4.18}$$

where,

$$\frac{ds}{d\xi} = |\frac{d\boldsymbol{x}_e}{d\xi}|\,.$$

The actual "infinite element" matrices are given by,

$$\begin{aligned} R_{kl}^1 &= \int_0^1 \xi^2\, \psi_k'\bar{\phi}_l'\, dx - \frac{1}{4}\int_0^1 \psi_k\bar{\phi}_l\, d\xi + \frac{1}{2}\psi_k(1)\bar{\phi}_l(1) \\ &\quad -ika\left[\int_0^1 (\psi_k'\bar{\phi}_l - \psi_k\bar{\phi}_l')\, dx - \psi_k(0)\bar{\phi}_l(0)\right]\,, \\ R_{kl}^2 &= \int_0^1 \psi_k\bar{\phi}_l\, d\xi\,. \end{aligned} \tag{4.19}$$

[1] Notice that integer $k$ is "overloaded".

Both 1D stiffness matrices are evaluated using standard Gaussian integration. As the order of the infinite elements may vary from an element to element, the order of mid-edge radial nodes is determined using the minimum rule. The element stiffness matrix is computed first for the element of a "complete" order, with the actual element matrices extracted from the complete stiffness matrix.

### Order of infinite element

The infinite elements in the initial mesh are assumed to be *isotropic*, i.e. order $N$ in the radial direction is set to the corresponding order $p$ of the edge on the truncating circle. The BC flag, stored for the corresponding mid-edge nodes is set to $900 + p$.

Typically, we begin with elements of second order. During the $hp$-refinements, edges on the truncating circle get $p$- or $h$-refined. Every time, the edge is $p$-refined, its IE radial order is updated, i.e. the BC flag is changed from $900 + p$ to $900 + p + 1$. We also update the IE order when the edge is $h$-refined as well, i.e. the *sons* of the edge are assigned the modified order BC flag $900 + p + 1$. Therefore, in presence of $h$-refinements, we encounter infinite elements with radial order *greater* than the FE order. This reflects the philosophy that any improvement in the approximation properties on the truncating circle, should be accompanied with the corresponding improvement in the radial direction as well.

In the presented experiments, the IE radial order has been restricted to $N \leq 9$.

# 5 Calculation of RCS

## 5.1 Direct evaluation using the IE solution

The simplest way to evaluate RCS is simply by using the shape functions (4.13). More precisely, if the direction $\hat{\boldsymbol{x}}$ intersects with a finite element edge (4.12) on the truncating circle, and $\xi_1$ is the value of the corresponding parameter, i.e.,

$$\frac{\boldsymbol{x}_e(\xi_1)}{|\boldsymbol{x}_e(\xi_1)|} = \hat{\boldsymbol{x}} \, ,$$

the corresponding formula is obtained by substituting in (4.13) $\xi_2 = 0$,

$$|\sum_k u_k \hat{\chi}_{i_k}(\xi_1)\hat{\psi}_{j_k}(0)| \, |\boldsymbol{x}_e(\xi_1)| \, . \tag{5.20}$$

Here, the summation extends over all IE shape functions (d.o.f.) $k$, $(i_k, j_k)$ denote the corresponding indices for the 1D FE shape functions $\hat{\chi}_i$ and radial trial functions $\psi_j$ constituting the IE shape function, and $u_k$ denote the IE d.o.f.

If, for instance, the IE formulation is stable in some suitable norm, formula (5.20) should give convergent results.

### 5.2 Evaluation through postprocessing

We shall limit our discussion to the 2D case. Any function $u$ that satisfies the Helmholtz equation in a domain exterior to a closed boundary $\Gamma$, along with the Sommerfeld radiation condition, satisfies automatically the *Helmholtz representation formula*,

$$u(\boldsymbol{x}) = \int_\Gamma \left\{ -\frac{\partial u}{\partial n}(\boldsymbol{y})\Phi(\boldsymbol{x},\boldsymbol{y}) + u(\boldsymbol{y})\frac{\partial \Phi}{\partial n}(\boldsymbol{x},\boldsymbol{y}) \right\} ds(\boldsymbol{y}) \,. \tag{5.21}$$

Here $\boldsymbol{n} = \boldsymbol{n}(\boldsymbol{y})$ is the unit normal directed to infinity, and $\Phi$ denotes the fundamental solution to the Helmholtz operator,

$$\Phi(\boldsymbol{x},\boldsymbol{y}) = \Phi(k|\boldsymbol{x}-\boldsymbol{y}|) \,,$$

where,

$$\Phi(kr) = \frac{H_0^{(2)}(kr)}{4i} \tag{5.22}$$

Here $H_0^{(2)}$ denotes the Hankel function of the second type, of order 0. Notice that changing the ansatz in time to $e^{-i\omega t}$, requires switching to the Hankel function of the first type.

Evaluating the normal derivative of the fundamental solution,

$$\frac{\partial \Phi}{\partial n}(\boldsymbol{x},\boldsymbol{y}) = k\,\Phi'(k|\boldsymbol{x}-\boldsymbol{y}|)\;\underbrace{\boldsymbol{n}(\boldsymbol{y})\cdot\frac{\boldsymbol{x}-\boldsymbol{y}}{|\boldsymbol{x}-\boldsymbol{y}|}}_{\cos\beta_y} \,,$$

we get,

$$u(\boldsymbol{x}) = \int_\Gamma \left\{ -\frac{\partial u}{\partial n}(\boldsymbol{y})\Phi(|\boldsymbol{x}-\boldsymbol{y}|) + k\,u(\boldsymbol{y})\Phi'(k|\boldsymbol{x}-\boldsymbol{y}|)\cos\beta_y \right\} ds(\boldsymbol{y}) \,. \tag{5.23}$$

Using the far field approximation,

$$|\boldsymbol{x}-\boldsymbol{y}| = |\boldsymbol{x}| - \boldsymbol{y}\cdot\hat{\boldsymbol{x}} \,,$$

and the asymptotic formula for the Hankel function and its derivative [1],

$$\Phi(kr) = i\sqrt{\frac{2}{\pi kr}}e^{-ikr}, \quad \Phi'(kr) = \sqrt{\frac{2}{\pi kr}}\,e^{-ikr},$$

we obtain,

$$\lim_{|\boldsymbol{x}|\to\infty} |\boldsymbol{x}|^{\frac{1}{2}}|u(\boldsymbol{x})| = \frac{1}{4}\sqrt{\frac{2}{\pi k}}\left| \int_\Gamma \left\{ -\frac{\partial u}{\partial n}(\boldsymbol{y}) + ik\,u(\boldsymbol{y})\boldsymbol{n}\cdot\hat{\boldsymbol{x}} \right\} e^{ik(\boldsymbol{y}\cdot\hat{\boldsymbol{x}})}\, ds(\boldsymbol{y}) \right| \,. \tag{5.24}$$

The integration can take place over *any contour* surrounding the scatterer. In context of the IE discretization, it is natural to integrate over the element edges adjacent to the truncating circle.

## 6 Numerical experiments

In all reported experiments, the error is computed in the $H^1$-semi-norm, integrated (only) over the computational domain. The error is reported in percent of the (semi)norm of the solution, defined over the same domain. The exact solution for the cylinder problem is computed using the Mie series. For the wedge problem, the unknown solution is replaced with the solution on the $hp$-refined mesh, see [6].

### Scattering of a plane wave on the rigid cylinder. Verification of the code

We begin with the standard comparison with the exact solution for the problem of scattering of a plane wave on a unit cylinder, see e.g. [9]. We set the wave number to $k = \pi$, and select the computational domain in the form of a ring with outer (the truncating circle) radius $a = 3$. Figure 2 displays convergence history for uniform and $hp$-adaptive refinements. As expected, the uniform $p$-refinements deliver exponential convergence, with the adaptive refinements delivering slightly smaller error but the same rates. Figure 3 shows

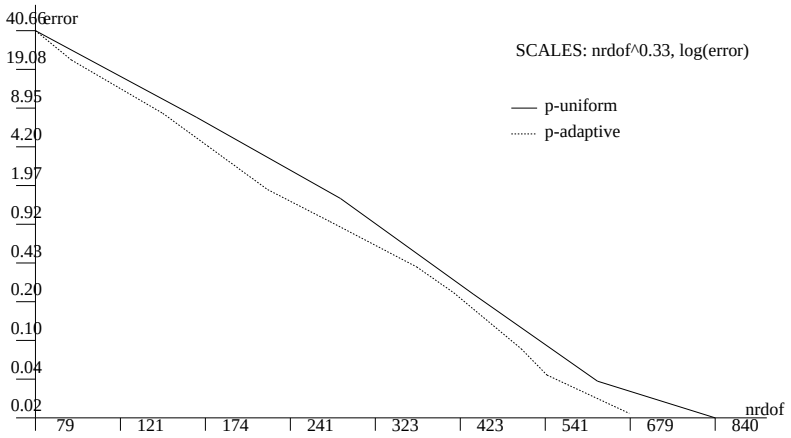


Figure 2: Scattering of a plane wave on a cylinder. Convergence history for uniform $p$- and adaptive $hp$ refinements

the optimal $hp$ mesh, corresponding to the error of 0.025 percent. Revealing are plots shown in Figures 4 and 5 presenting contour lines of the real (range: -0.62958E-02 0.57420E-02 ) and imaginary (range: -0.47019E-02 0.45273E-02) parts of the error function, for the uniform mesh of quartic elements. The graph display a portion of the infinite elements corresponding to $\frac{1}{2} < \xi_2 < 1$. The solution in the IE domain is actually better than in the finite element domain which seems to be consistent with the fact that the method seems to be stable in $L^1$ norm *after taking out the Jacobian* (see the discussion in Section 3). Finally, for the same mesh of quartic elements (1.5 percent error), Figure 6 presents the monostatic RCS corresponding to range from 180 to 0 degrees (left to right), displayed in dB (20 log of the actual value). Both methods for computing RCS yield identical results (first three significant digits accurate). The derivatives in formula (5.24) have been averaged over the adjacent finite and infinite elements. With the derivatives evaluated using only the contributions from either finite or infinite elements, the corresponding value of RCS differs in the third digit. In this sense the first approach seems to deliver better results which is quite remarkable. The slight variations of the RCS for the cylinder reflect the imperfect approximation of the geometry.

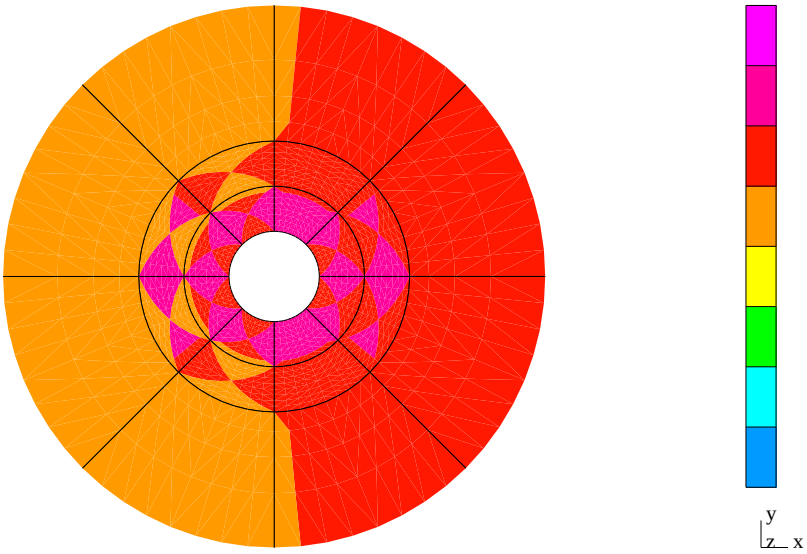


Figure 3: Scattering of a plane wave on a cylinder. Optimal $hp$ mesh corresponding to 0.025 percent error

### Comparison of Bubnov- and Petrov-Galerkin formulations

Fig. 7 displays the convergence history for the automatic $hp$-adaptivity, and the two versions of the infinite element test functions. The Petrov-Galerkin version delivers slightly better results for coarse meshes but the differences are insignificant. Both methods seem to display the same character of convergence. In particular, the RCS computations discussed above yield identical results (first three digits coincide). Same conclusions apply to the wedge problem discussed next.

### Scattering of a plane wave on a wedge

The second and final example deals withe the resolution of singularities, and its impact on RCS. We have divided the cylinder from the previous example into four equal quadrants and kept just one of them. We set the wave number $k = \pi$, i.e. the distance between the truncating boundary and the object is equal to one wavelength. Just as an example, Figures 8 and 9 present the optimal $hp$ mesh with zooms on one of the corners for the rather academic error level of 0.1 percent. Fig. 10 presents the convergence histories for the problem using both Bubnov- and Petrov-Galerkin formulations. Similarly to the cylinder problem, the differences are insignificant although, again, the Petrov- Galerkin method seems to be doing a little better.

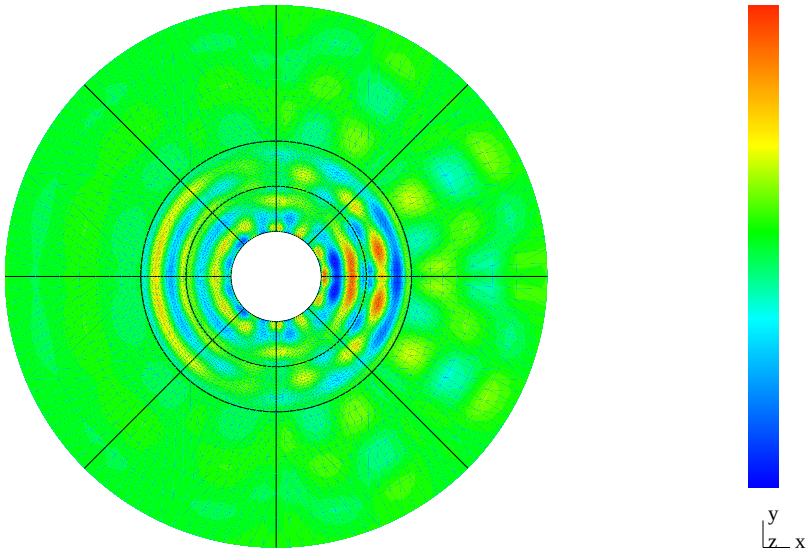


Figure 4: Scattering of a plane wave on a cylinder. Real part of the error function for a uniform mesh of quartic elements

### Does the resolution of singularities matter ?

We come to the final experiment reflecting the impact of adaptivity on evaluation of RCS. Figure 11 presents RCS for the wedge problem evaluated using a uniform mesh of quartic elements and $hp$-adaptive meshes. The choice of the uniform meshes reflects the usual practice in selecting a mesh that reproduces the wave form of the solution (two quartic elements per wavelength) and delivers an error in the range of 3-4 percent. The $hp$ meshes were obtained by requesting a one percent error level, at which several levels of $hp$-refinements resolve the structure of the singularities in the solution. For each direction of the incoming wave ($\theta = 180, 179, \ldots, 0$, left to right), the $hp$-adaptive algorithm was run starting with the optimal mesh for the previous direction, with the optimization procedure restarted from the initial mesh every 10 degrees. The result is discouraging for those "selling" adaptivity. Except for a slight shift in the RCS level, the results are practically identical. Resolution of the singularity seems to be insignificant.

On the positive (for adaptivity) side, the same error level of roughly 3.5 percent, and the quality of the corresponding RCS, can be obtained with meshes roughly half the size of the uniform meshes. Figure 12 presents an example of such a mesh for the direction of 90 degrees. Again, the fact that the algorithm selected only $p$-refinements, indicates that, at this error level, the resolution of singularities does not matter.

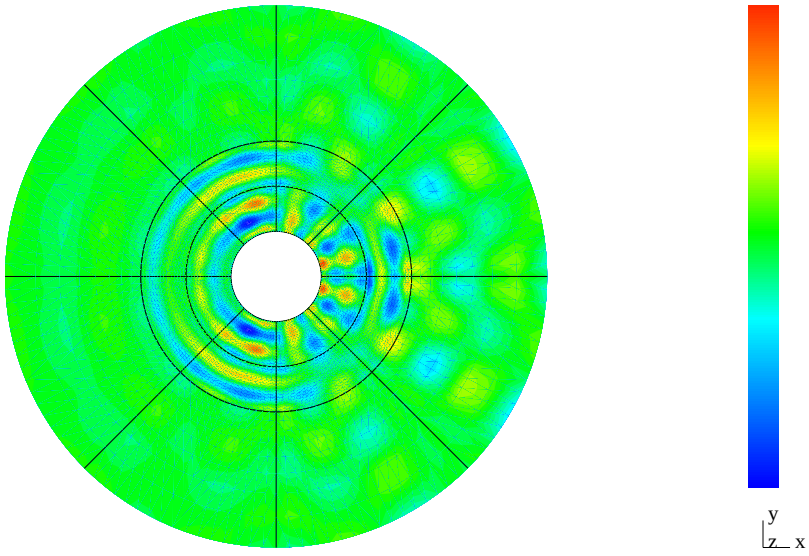


Figure 5: Scattering of a plane wave on a cylinder. Imaginary part of the error function for a uniform mesh of quartic elements

### Evaluation of RCS

Both methods of evaluating RCS seem to deliver practically the same results and converge with the same rates. The direct method seems to be doing a bit better as illustrated in Fig. 13.

## 7 Conclusions

We summarize the main conclusions of our brief considerations and numerical experiments.

1. Interpreting the calculation of the sesquilinear form in the CPV sense, allows for a symmetric choice of trial and test shape functions. The choice does not seem to have any impact on the convergence properties. Will the symmetric choice be easier to analyze in terms of convergence proofs?

2. Both formulation allow for a direct evaluation of RCS from the IE representation of the solution. The method seems to converge uniformly in the whole exterior domain.

3. The use of locally variable order of IE approximation is possible. The infinite element can be used in conjunction with the automatic $hp$-adaptivity.

4. Resolution of singularities seem to have little impact on the RCS calculations, although adaptivity (ideally goal-driven) allows for essential savings in terms of problem size.

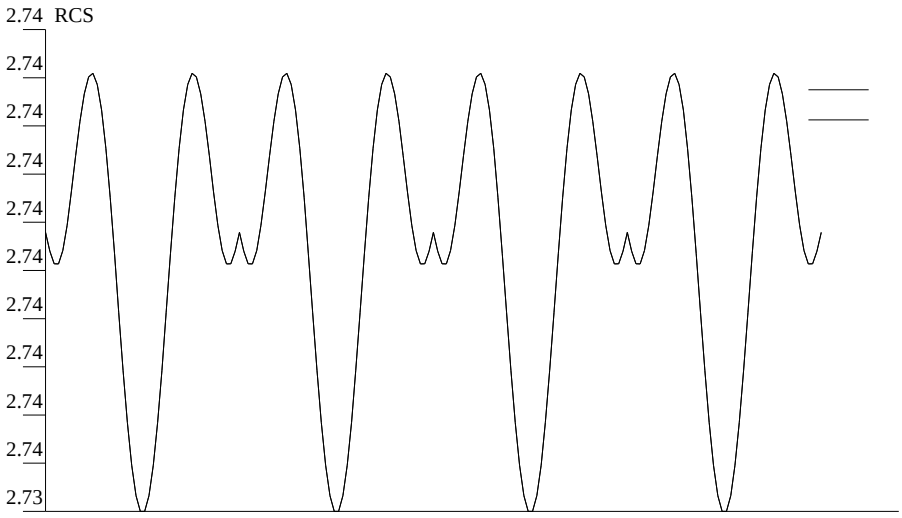


Figure 6: Scattering of a plane wave on a cylinder. RCS for the uniform mesh of quartic elements (1.5 percent error)

5. The most important difference between the adaptive and non-adaptive techniques comes with the fact that the adapted mesh comes with an error estimate guaranteeing the quality of the delivered numerical result.

The $hp$ code used in the presented experiments can be downloaded from

http://www.ticam.utexas.edu/%7Eleszek/hp-intro.html

# References

[1] *Handbook of Mathematical Functions, with Formulas, Graphs and Mathematical Tables*. Edited by Milton Abramowitz and Irene A. Stegun. Fifth printing, with corrections. National Bureau of Standards Applied Mathematics Series, Vol. 55. National Bureau of Standards, Washington 1966.

[2] T. Z. Boulmezaoud, "Inverted Finite Elements: a New Method for Solving Elliptic Problems in Unbounded Domains", *Mathematical Modeling and Numerical Analysis* ($M^2AN$), to appear.

[3] W. Cecot, L. Demkowicz, and W. Rachowicz, "A Two-Dimensional Infinite Element for Maxwell's Equations", *Computer Methods in Applied Mechanics and Engineering*, **188**, 625-643, 2000.

[4] L. Demkowicz, *Computing with $hp$ Elements*, in preparation.

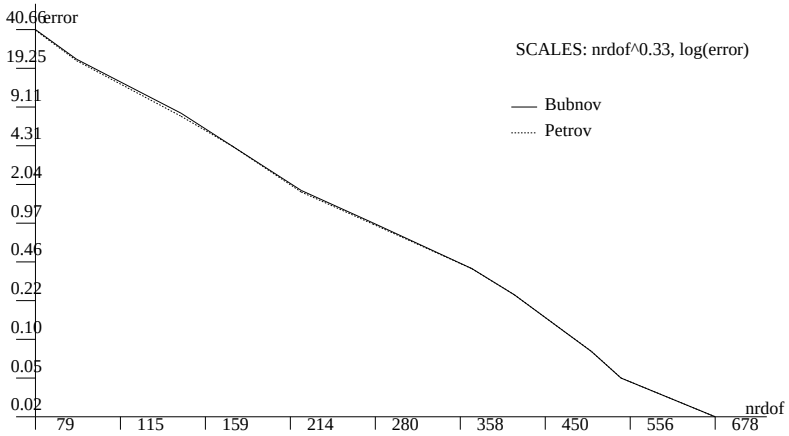


Figure 7: Scattering of a plane wave on a cylinder. Convergence history for adaptive $hp$ refinements using Bubnov- and Petrov-Galerkin IE formulations


[5] L. Demkowicz and F. Ihlenburg, "Analysis of a Coupled Finite-Infinite Element Method for Exterior Helmholtz Problems", *Numerische Mathematik*, **88**, 43-73, 2001.

[6] L. Demkowicz, W. Rachowicz, and Ph. Devloo, "A Fully Automatic hp-Adaptivity", *Journal of Scientific Computing*; **17**(1-3): 127-155.

[7] L. Demkowicz, "2D $hp$-Adaptive Finite Element Package (2Dhp90). Version 2.1", *TICAM Report 02-06*.

[8] Benyu Guo, Jie Shen and Zhongqing Wang, "A rational approximation and its applications to differential equations on the half line", *J. Sci. Comp.*, **15**, 117-147, 2000.

[9] M. C. Junger, and D. Feit, *Sound, Structures, and Their Interaction*, MIT Press, Boston 1986.

[10] D. Pardo, L. Demkowicz, C. Torres-Verdin, L. Tabarovsky, "A Goal-Oriented hp-Adaptive Finite Element Method with Electromagnetic Applications. Part I: Electrostatics.", *ICES Report 04-57*.

[11] A. Safjan, M. Newman, "On Two-Dimensional Infinite Elements Utilizing Basis Functions with Compact Support", *Computer Methods in Applied Mechanics and Engineering*, **190**, 48, 6399-6424, 2001.

[12] P. Solin, L. Demkowicz, "Goal-Oriented hp-Adaptivity for Elliptic Problems", *Computer Methods in Applied Mechanics and Engineering*, **193**, 44-468, 2004.

[13] A. Zdunek, and W. Rachowicz, "A Three-dimensional $hp$-Adaptive Finite Element Approach to Radar Scattering Problems", *Fifth World Congress on Computational Mechanics* Vienna, Austria, 7-12 July, 2002.

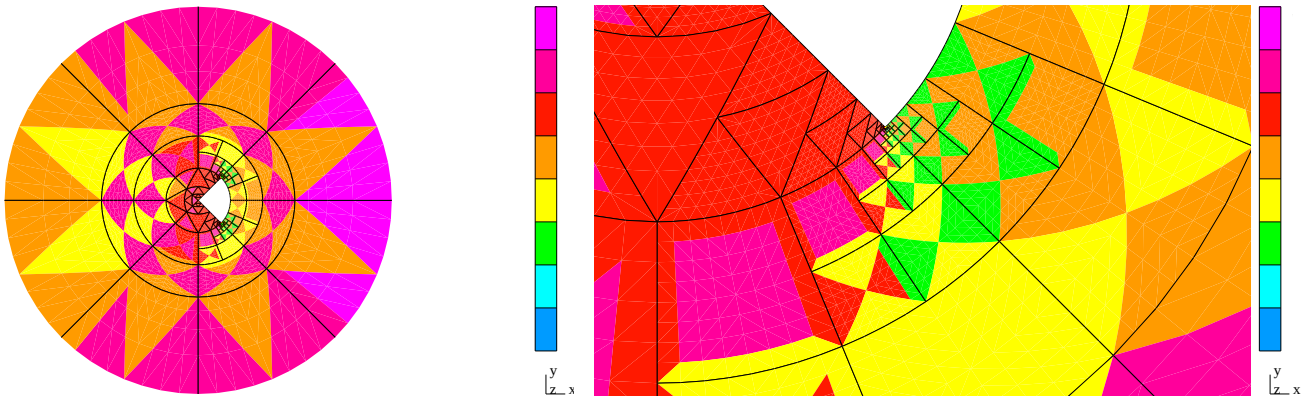

Figure 8: Scattering of a plane wave on a wedge. Optimal $hp$ mesh for 0.1 percent error, with a 10 times zoom on the lower corner

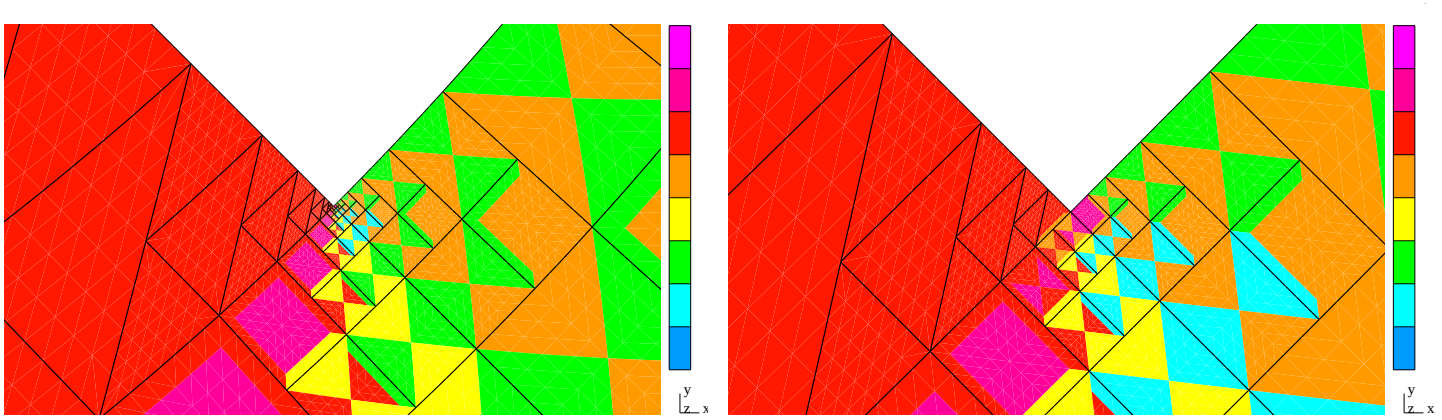

Figure 9: Scattering of a plane wave on a wedge. Optimal $hp$ mesh for 0.1 percent error. Zooms on the lower corner with 100 and 1000 magnifications

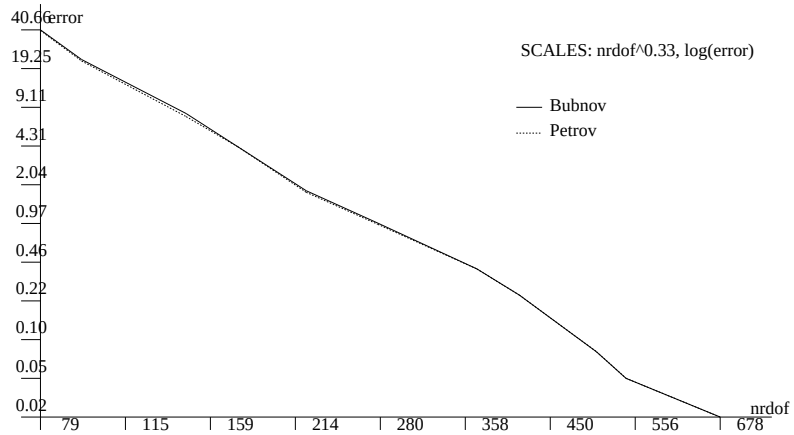


Figure 10: Scattering of a plane wave on a wedge. Convergence history for adaptive $hp$ refinements using Bubnov- and Petrov-Galerkin IE formulations

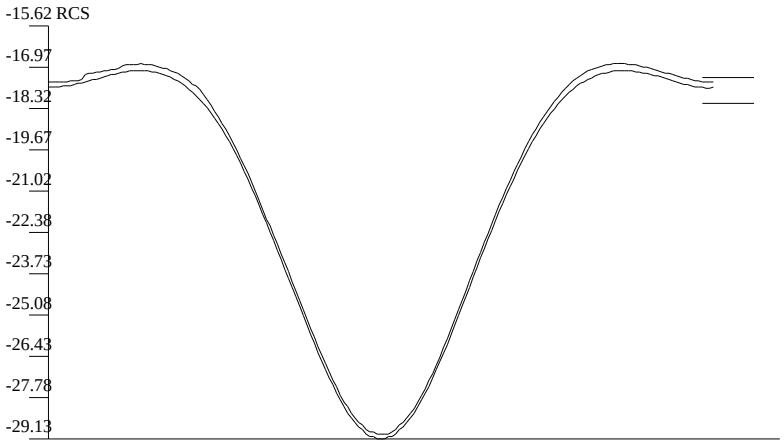


Figure 11: Scattering of a plane wave on a wedge. RCS for the uniform mesh of quartic elements (3-4 percent error range level) and $hp$-adaptive mesh (1 percent error)

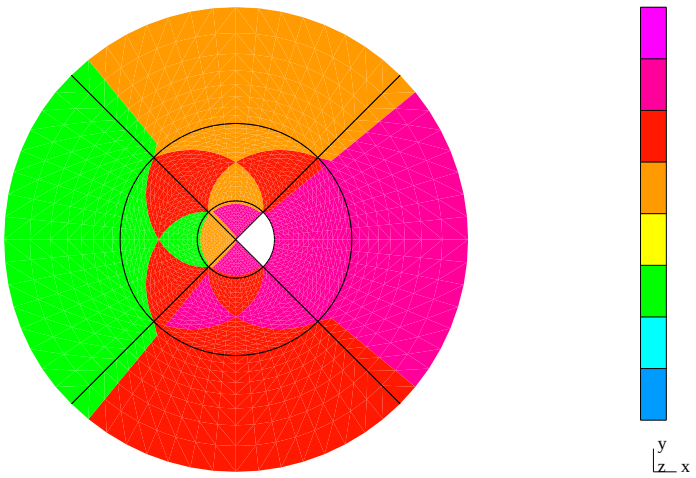


Figure 12: Scattering of a plane wave on a wedge. Optimal $hp$ mesh for the direction of 90 degrees

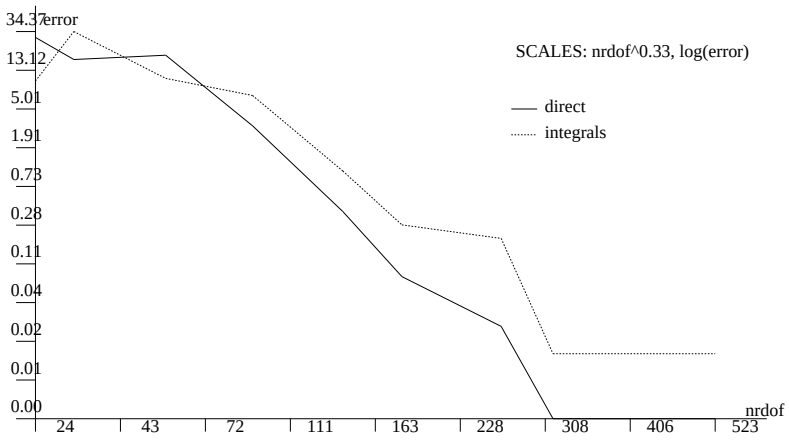


Figure 13: Scattering of a plane wave on a cylinder. Convergence of the RCS evaluated using the two methods